INVITED REVIEW OPEN ACCESS

Magnetic Resonance Myocardial Imaging in Patients With Implantable Cardiac Devices: Challenges, Techniques, and Clinical Applications

Pauline Gut[1,2] | Hubert Cochet[1,3] | Matthias Stuber[1,2,4] | Aurélien Bustin[1,2,3]

[1]IHU LIRYC, Heart Rhythm Disease Institute, Université de Bordeaux – INSERM U1045, Pessac, France | [2]Department of Diagnostic and Interventional Radiology, Lausanne University Hospital and University of Lausanne, Lausanne, Switzerland | [3]Department of Cardiovascular Imaging, Hôpital Cardiologique du Haut-Lévêque, CHU de Bordeaux, Pessac, France | [4]CIBM Center for Biomedical Imaging, Lausanne, Switzerland

Correspondence: Aurélien Bustin (aurelien.bustin@ihu-liryc.fr)

ABSTRACT

Cardiovascular magnetic resonance imaging (MRI) in patients with cardiac implants, such as pacemakers and defibrillators, has gained importance in recent years with the development of modern cardiac implantable electronic devices. The increasing clinical need to perform MRI examinations in patients with cardiac implants has driven the development of new advanced MRI sequences to mitigate image artifacts associated with cardiac implants. More specifically, advances in imaging techniques, such as wideband late gadolinium enhancement imaging, wideband T1 mapping, and wideband perfusion, have been designed to improve image quality and examinations in patients with cardiac implants, enabling a comprehensive and more reliable diagnosis, which was previously unattainable in these patients. This review article explores recent developments and applications of wideband techniques in the field of cardiovascular MRI, offering insights into their transformative potential. Clinical applications of wideband cardiovascular MRI are highlighted, particularly in assessing myocardial viability, guiding ventricular tachycardia ablation, and characterizing myocardial tissue.

1 | Background

Cardiovascular magnetic resonance (CMR) imaging has become an essential diagnostic tool due to its ability to generate high-resolution images of soft tissues without ionizing radiation. It has the unique capability of identifying tissue-based mechanisms underlying various cardiac conditions, including congenital heart disease, cardiomyopathies, and ischemic heart disease. The use of cardiac implantable electronic devices (CIEDs), such as pacemakers, transvenous (TV) implantable cardioverter defibrillators (ICDs), subcutaneous (S) ICDs, cardiac resynchronization therapy (CRT) devices, and implantable loop recorders (ILRs), has been increasing over the past decades [1, 2], with approximately 1.4 million implantations occurring worldwide each year [3],

to treat arrhythmias, heart failure, and prevent sudden cardiac death [4, 5]. The prevalence of patients with CIEDs undergoing CMR has also increased over the past decades [6]. Approximately 50%–70% of patients with CIEDs will require follow-up magnetic resonance imaging (MRI) scans throughout their lifetime [7].

Historically, the presence of CIEDs complicated the use of MRI due to their interactions with the MRI environment and were widely considered an absolute contraindication to MRI. Since 2000, with the development of modern CIEDs [8], many studies have shown that MRI can be performed with relatively low risk in both MR-conditional and non-MR-conditional CIEDs at 1.5 T [9–14] using well-designed protocols [15–17]. Although MRI can be safely performed at 1.5 T for patients who are not device-dependent [10–12, 18], CIEDs can cause various artifacts, such as signal loss, signal pileup (hyperintensity), failure of fat suppression, ineffective signal nulling, and image distortion. These artifacts result from differences in magnetic susceptibility between the implants and adjacent soft tissues, compromising the image and limiting its interpretation and diagnosis [19–21].

In this review, we discuss the current state-of-the-art in the field of wideband CMR, its advantages, challenges, and clinical applications, to provide researchers and clinicians with an overview of the different techniques used to image and quantify the myocardium in the presence of CIEDs.

2 | The Challenges of MRI for Patients With CIED

2.1 | Safety

The American Society for Testing and Materials (ASTM) has classified biomedical implants and devices used in the MRI environment into three groups since 2005: (i) MR safe, (ii) MR conditional, and (iii) MR unsafe [22]. No CIED can be classified as MR safe; they are either MR conditional or MR non-conditional. An MR conditional CIED implies that all components, including the leads and generator, are MR conditional; if one part is non-conditional, the device is classified as MR non-conditional. MR conditional CIEDs indicate that the device presents no known risks or hazards in a specific MRI environment.

Before the 2000s, CIEDs were considered an absolute contraindication for MRI. However, with the development of modern devices (manufactured after 2000) [8], that are small, have less magnetic material, and have improved electromagnetic interference safety, many studies in patients with MR conditional and MR non-conditional CIEDs have demonstrated that MRI can be safely performed at 1.5 T, following specific protocols and intraprocedural programming of the device [9, 10, 11, 13, 23–25]. However, the presence of fractured, abandoned, or epicardial leads remains a contraindication for performing MRI [24, 25].

2.2 | Potential Adverse Effects

2.2.1 | Device Malfunction

Strong radiofrequency (RF) and gradient fields can induce electrical currents in the leads of CIEDs, potentially triggering various atrial or ventricular arrhythmias. Electromagnetic interference can cause device malfunction by altering its pacing mode (e.g., asynchronous pacing or inhibition of tachycardia), resulting in inappropriate pacing, inhibition of pacing, or false sensing. This can lead to over- or undersensing, which interferes with proper pacing or tachyarrhythmia therapies [26]. These issues can be detected through adequate patient monitoring during CMR. Nevertheless, to avoid potential adverse effects, pacemakers should be set to asynchronous mode (VOO or DOO) in dependent patients or inhibited mode (VVI or DDI) in non-dependent patients before undergoing MRI. Additionally, ICDs should be deactivated for tachyarrhythmia therapy (ATP/shock) and reprogrammed to inhibited mode (VVI/DDI) [10, 11].

2.2.2 | Heating

Electrode heating occurs due to the resonant coupling of the electric field with the wire, known as the antenna effect. This effect can lead to heat deposition at the lead-tissue interface, potentially damaging the tissue and modifying pacing thresholds, which may induce or result in the loss of arrhythmia capture. Fractured, epicardial, and abandoned electrode leads are particularly sensitive to the effects of heating [27].

2.2.3 | Torque

Torque from magnetic field interactions can cause movement or dislocation of ferromagnetic implants [28] and is proportional to the magnetic field strength [26]. Modern devices and leads are designed with minimal ferromagnetic components, making them unlikely to experience significant movement [29].

2.3 | Device-Related Artifacts

The positive susceptibility in ferromagnetic components of CIEDs produces local inhomogeneities of the static B0 and RF B1 fields, affecting the phase and frequency of nearby protons [30, 31], which results in various types of image artifacts discussed below (Figure 1). CIED-related artifacts are influenced by the size of the device generator and its distance from the heart, as well as by the leads [32, 33].

2.3.1 | Signal Loss

A significant variation in the local magnetic field within a voxel can occur in the vicinity of CIEDs and can lead to rapid dephasing and incoherence of the intravoxel spins, also known as the T2* effect, which appears as a dark zone of signal void surrounding the CIED. Signal loss can also occur due to the failure to excite spins resonating at a frequency outside the bandwidth of the RF pulse [30, 31].

2.3.2 | Spatial Misregistration

Local variations in the B0 field lead to a dispersion of the Larmor frequencies of the spins. Spins located outside the slice of
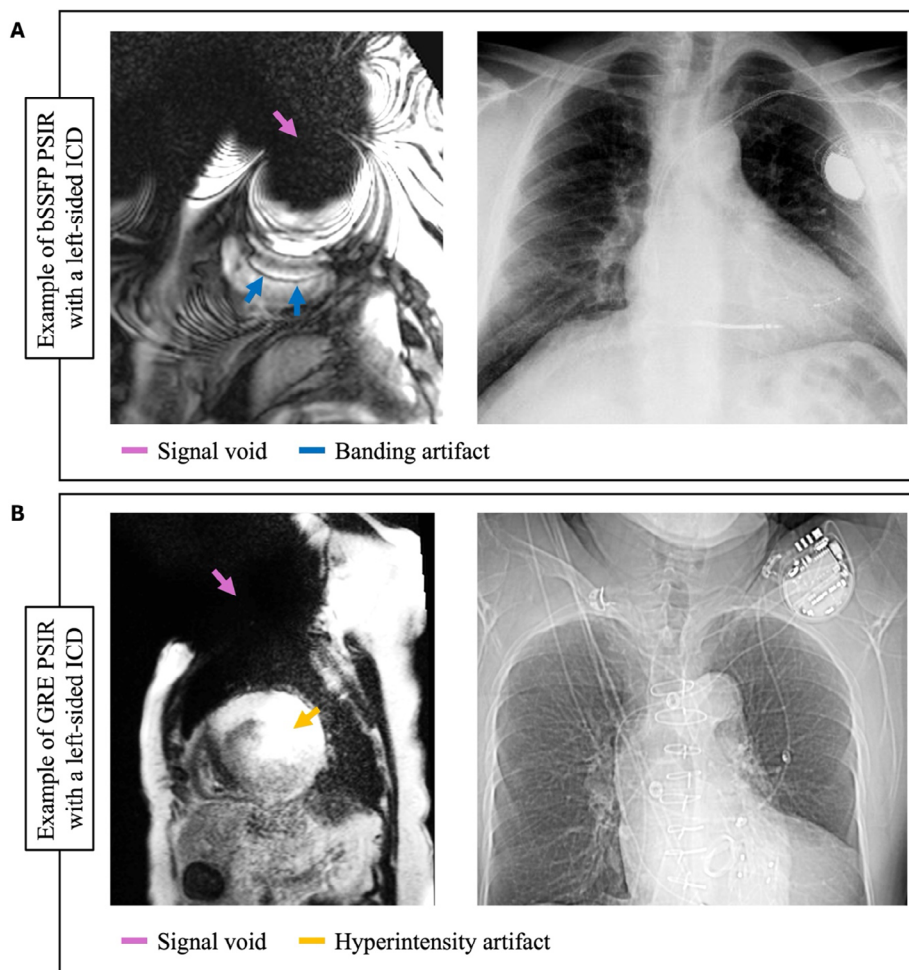
FIGURE 1 | Example of CIED-related artifacts. (A) Signal void (purple) and bSSFP-associated banding artifacts (blue) are observed using a bSSFP PSIR LGE sequence in the presence of a left-sided ICD (x-ray). (B) Signal void (purple) and bSSFP-associated banding artifacts (blue) are observed using a GRE PSIR LGE sequence in the presence of a left-sided ICD (x-ray). bSSFP, balanced steady-state free-precession; CIED, cardiac implantable electronic device; GRE, gradient recalled echo; ICD, implantable cardioverter defibrillator; LGE, late gadolinium enhancement; PSIR, phase-sensitive inversion recovery.

interest may be excited due to changes in precession frequency, erroneously contributing to the image. Additionally, during readout, voxels may be registered at incorrect locations along the frequency encoding direction, altering image reconstruction and causing signal loss, signal pileup, and geometric distortion [30, 31]. Furthermore, spins with altered precession frequency may not be correctly excited or tipped using MRI sequences with magnetization preparation, as is the case for inversion recovery (IR) or saturation recovery (SR).

2.3.3 | Fat Suppression

Spectrally selective fat-signal suppression techniques rely on the homogeneous resonance of protons and the different resonance frequencies of fat and water, known as chemical shift. RF fat suppression pulses target the fat resonance frequency to selectively suppress the fat signal. However, CIED-related local B0 inhomogeneities can affect the resonance frequency of nearby fat protons, shifting the fat peak outside the RF pulse bandwidth and leading to inadequate fat suppression. Protons that do not

resonate at the expected frequency may escape suppression. Additionally, water protons may resonate at a frequency close to that of fat and be erroneously suppressed, causing unintended signal loss [30, 31].

Water excitation is a method that selectively excites water protons inside a section using section-selective composite pulses and leaves fat protons unaltered [34]. Local B0 inhomogeneities linked to CIED can affect the resonance frequency of nearby water protons, leading to inadequate water excitation. Additionally, fat protons may resonate at a frequency close to that of water and be erroneously excited.

2.3.4 | Device Location

The severity of image artifacts due to the presence of CIEDs depends on the location and size of the device generator as well as the leads [32]. Pacemakers and right-sided ICDs generally cause minimal image artifacts in CMR. In contrast, left-sided ICDs are more problematic for CMR. Additionally, transvenous

implantable cardioverter defibrillator (TV-ICD) pulse generators are typically placed in the upper chest, with an additional pacing lead in the coronary sinus for CRT-Ds, while subcutaneous implantable cardioverter defibrillators (S-ICDs) are placed in the left mid-axillary line with a lead tunneled along the left subcostal margin. Consequently, CRT-Ds and S-ICDs tend to produce more severe artifacts than TV-ICDs, with S-ICDs generally causing the most severe artifacts [35].

3 | Technical Adjustments

Various studies have proposed strategies for reducing CIED-related artifacts in MR images by optimizing the imaging protocol [30, 31, 36], as summarized in Table 1.

3.1 | Field Strength

When placed in an external magnetic field B0, ferromagnetic materials are strongly magnetized in the direction of the field as they have a positive magnetic susceptibility. The density of the field lines of force increases within the ferromagnetic material, producing a local distortion of the magnetic field around the metallic object. This variation in the magnetic field induces a small magnetic field gradient between the metallic object and surrounding tissues of different susceptibility, resulting in local field inhomogeneities that may lead to susceptibility artifacts. The severity of susceptibility artifacts induced by these local field inhomogeneities is linearly proportional to the strength of the main magnetic field B0. Consequently, images obtained with a CIED at 1.5 T will show reduced artifacts when compared to 3 T. Therefore, it is preferable to perform MRI at a lower field strength in the presence of CIEDs. New low-field systems, such as 0.55 T MRI, may therefore offer significant potential to further reduce susceptibility artifacts, but future studies need to assess safety and image quality in patients with CIEDs.

3.2 | Patient Position

The extent of field inhomogeneities caused by the presence of CIEDs is related to the spatial position of the spins relative to the device. Increasing the distance between the CIED and the heart can help reduce artifacts in the myocardium. This can be achieved by raising the left arm ipsilaterally close to the head for patients with a left-sided CIED implant [24] and acquiring images during inspiration rather than expiration. For example, in 2022, Vuorinen et al. [37] reported a 25% increase in artifact-free segments using arm-raised imaging.

3.3 | Sequence Parameters

In accordance with the 2024 SCMR consensus [24] and the work of Lee et al. [31], CIED-related artifacts can be considerably reduced by optimizing MRI sequences. First, sequences sensitive to off-resonance should be avoided. Balanced steady-state free-precession (bSSFP) sequences should be replaced with gradient recalled echo (GRE) sequences. Although blood-myocardial contrast and signal-to-noise ratio (SNR) are reduced, banding artifacts that arise in bSSFP sequences in the presence of CIEDs are less dominant on images acquired with GRE sequences. Additionally, signal dephasing can be mitigated by using smaller voxel sizes (reducing slice thickness and increasing matrix size) and shorter echo times. A shorter echo time can be achieved by using a shorter RF pulse, a higher receiver bandwidth, and a fractional echo. Another consideration is using a larger readout bandwidth to reduce geometric distortion occurring in the frequency-encoding direction. However, such bandwidth increase comes at the expense of a loss in SNR.

Despite these solutions for attenuating image artifacts in CIED patients, they may be insufficient, especially when using magnetization-prepared sequences, such as phase-sensitive inversion recovery (PSIR) [38]. The following sections focus on techniques specific to magnetization-prepared sequences for mitigating CIED-related artifacts.

4 | Adiabatic Pulses

CIEDs produce field inhomogeneities, and adiabatic pulses are commonly employed because they are less sensitive to B0 and B1 inhomogeneities. Below is a succinct description of adiabatic pulses.

4.1 | Adiabatic Radiofrequency Pulses

An adiabatic pulse [39, 40] is a type of RF pulse characterized by a time-varying frequency, modulated amplitude, and modulated phase, while satisfying the adiabatic condition. Across the spectral bandwidth of the adiabatic pulse, spins with different resonant frequencies (isochromats) are sequentially rotated as the frequency sweep of the RF pulse approaches the resonance frequency of each isochromat. Unlike an ordinary amplitude-modulated rectangular RF pulse, where all isochromats are affected simultaneously, an adiabatic RF pulse manipulates each isochromat at different times. An adiabatic RF pulse is designed so that the net magnetization adiabatically follows the effective magnetic field, which combines the static magnetic field B0 and the time-varying RF magnetic field B1 (Figure 2). In other words, the net magnetization gradually adjusts its orientation to remain aligned with the effective magnetic field throughout the duration of the adiabatic RF pulse. Consequently, for spins precessing within the frequency band of the adiabatic RF pulse, the flip angle remains uniform because the orientation of the effective magnetic field changes more slowly than the rotation of the net magnetization around this effective field. This adherence to the adiabatic condition ensures that the magnetization vector can continuously adjust its orientation to stay aligned with the effective field. The rate of change of the effective magnetic field direction (θ) must be slow compared to the precession frequency of the magnetization around the effective field (ω_{eff}). Mathematically, the adiabatic condition can be expressed as a

**TABLE 1** | Overview of technical developments in wideband cardiovascular resonance magnetic imaging.

Publication	Purpose	Wideband RF pulses	Readout	Resolution Slice thickness Flip angle Bandwidth
Rashid et al. 2014 [42]	2D wideband IR LGE at 1.5 T	IR: HS, BW = 3.8 kHz (μ = 16, β = 750, duration = 10.24 ms)	Cartesian GRE Breath-hold	1.4×1.9 mm^2 8 mm 25° 500 Hz/pixel
Ranjan et al. 2015 [69]	2D wideband IR LGE at 3 T	IR: HS, BW = 3.8 kHz (μ = 10, β = 750, duration = 6.1 ms)	Cartesian GRAPPA x2 GRE Breath-hold	1.5×1.5 mm^2 7 mm 20° 744 Hz/pixel
Hong et al. 2015 [80]	2D wideband AIR T1 mapping at 1.5 T	BISTRO SR: 15 HS, BW = 8.9 kHz (μ = 10, β = 750, duration = 3.07 ms)	Cartesian GRAPPA x2 GRE Breath-hold	2.8×2.8 mm^2 8 mm 10° 1000 Hz/pixel
Rashid et al. 2016 [43]	3D wideband IR LGE at 1.5 T	IR: HS, BW = 3.8 kHz (μ = 16, β = 750, duration = 10.24 ms) Excitation: sinc, BW = 12 kHz (BWT = 7.2, duration = 600 μs)	Cartesian GRE Respiratory-navigated	$1.4 \times 1.4 \times 4$ mm^3 – 20° 500–1000 Hz/pixel
Shao et al. 2017 [44]	2D wideband MOLLI T1 mapping at 1.5 T	IR: HS, BW = 3.8 kHz (μ = 16, β = 750, duration = [100, 180, 260] ms)	Cartesian GRAPPA x2 GRE Breath-hold	1.9×1.9 mm^2 8 mm 10° 502 Hz/pixel
Hong et al. 2019 [87]	2D wideband MOCO perfusion at 1.5 T	BISTRO SR: HS, BW = 9.2 kHz (μ = 10, β = 750, duration = 2.82 ms)	Cartesian GRAPPA x2 GRE Free-breathing with MOCO	1.9×1.9 mm^2 8 mm 15° 745 Hz/pixel
Hong et al. 2020 [88]	Accelerated 2D MOCO wideband perfusion at 1.5 T	SR: 3 HS, BW = 9.2 kHz (μ = 10, β = 750, duration = 2.82 ms)	Cartesian Five-fold accelerated with variable density and CS GRE Free-breathing with MOCO	2.1×2.1 mm^2 8 mm 15° 740 Hz/pixel
Gut et al. 2024 [45]	2D wideband IR-T2prep black-blood LGE at 1.5 T	IR: HS, BW = 3.8 kHz (μ = 16, β = 750, duration = 10.24 ms) T2 refoc: HS, BW = 5.0 kHz (μ = 25, β = 785, duration = 12.8 ms)	Cartesian GRAPPA x2 GRE Breath-hold	1.4×1.4 mm^2 8 mm 20° 751 Hz/pixel
Hong et al. 2024 [75]	Accelerated 3D wideband IR LGE at 1.5 T	IR: HS, BW = 4 kHz	Stack-of-stars XD-GRASP GRE 2D self-navigation	1.5-2 $\times$ 1.5-2 $\times$ 1.5-2 mm^3 – 15°–18° 400–600 Hz/pixel

Abbreviations: AIR, arrhythmia-insensitive rapid; BISTRO, B1-insensitive train to obliterate signal; BW, spectral bandiwdth; BWT, bandwidth-time-product; CS, compressed sensing; GRE, gradient recalled echo; HS, hyperbolic secant; IR, inversion recovery; LGE, late gadolinium enhancement; MOLLI, modified Look-Locker inversion-recovery; T2 refoc, T2 preparation refocusing pulse.

function of time (t):

$$\left| \frac{d\theta(t)}{dt} \right| \leq \omega_{\text{eff}}(t)$$

Adiabatic RF pulses are relatively insensitive to B1 inhomogeneities and frequency offsets, making them particularly useful in situations where the magnetic field is inhomogeneous. Several types of adiabatic RF pulses exist [39–41], such as hyperbolic secant (HS), tangent hyperbolic secant, WURST, and BIR, each with distinct characteristics. In the context of late gadolinium
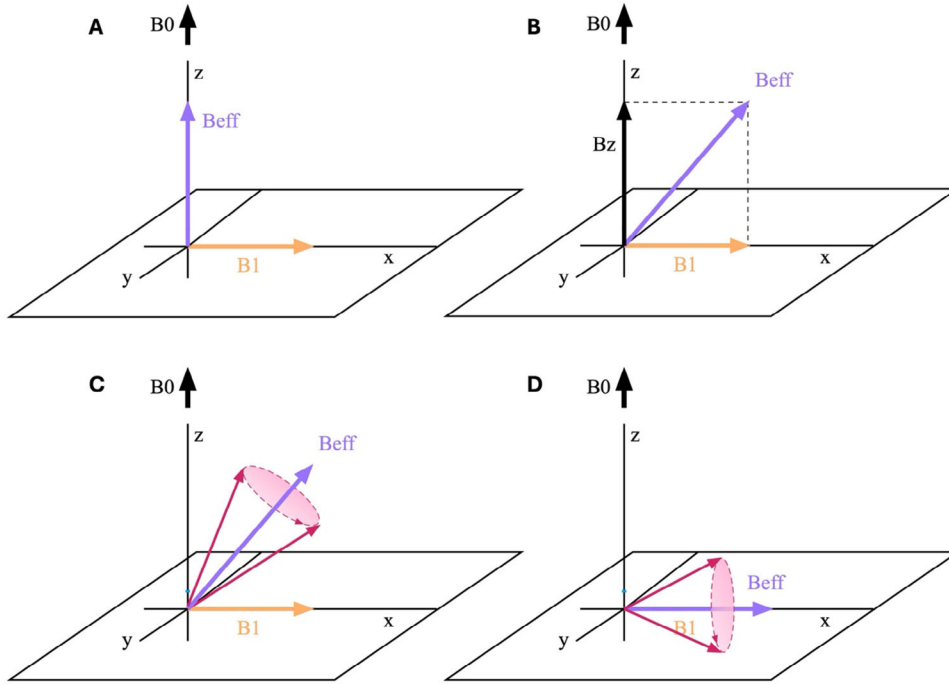
FIGURE 2 | Example of an adiabatic excitation. The initial magnetization is along the initial axis of the effective field Beff (A). If the adiabatic condition is met, meaning the radiofrequency B1 field is applied slowly enough, the magnetization will gradually follow Beff during the frequency sweep (B) and the magnetization will precess around Beff (C). When the radiofrequency B1 field has swept to the resonance frequency, the magnetization will be rotated to 90° (D).

enhancement (LGE) cardiac MRI, the HS type is commonly used for IR [42–45].

4.2 | Adiabatic Hyperbolic Secant IR Pulses

An adiabatic HS pulse [39, 40, 46] with duration T_p, amplitude modulation $A(t)$ and phase modulation $\Phi(t)$ is given by:

$$\mathrm{B1}\ (t) = A(t)\ e^{i\ \Phi(t)}$$

$$A\ (t) = A_0\ \sec h\ (\beta t)$$

$$\Phi\ (t) = \mu \ln\left(\sec h\ (\beta t)\right)$$

for $-T_\mathrm{p}/2 \leq t \leq T_\mathrm{p}/2$, where A_0 is the maximum B1 field amplitude, β is a frequency modulation parameter in radians per second, and μ is the degree of phase modulation (dimensionless).

The frequency modulation function $\Delta\omega(t)$ is calculated by taking the time derivative of the phase modulation:

$$\Delta\omega\ (t) = \frac{d\Phi(t)}{dt} = -\mu\beta \tan(\beta t)$$

To design an adiabatic HS IR pulse, A_0, μ, and β need to be determined. To fulfill the adiabatic passage condition, the peak

B1 amplitude A_0 must satisfy the following condition:

$$A_0 \geq \frac{\mu \sqrt{\beta}}{\gamma}$$

The RF spectral bandwidth Δf of an HS pulse is given by:

$$\Delta f = \frac{\mu\beta}{\pi}$$

To fulfill the adiabatic condition, HS pulses require higher B1 amplitudes for wider bandwidths. The minimum B1 amplitude required for an adiabatic HS pulse scales linearly with μ but only as the square root of β. Therefore, a smaller increase in μ and a larger increase in β can achieve a certain bandwidth without a dramatic increase in the B1 amplitude A_0.

5 | Wideband CMR: Technical Developments

5.1 | Inversion and Saturation

5.1.1 | Technical Challenges

IR or SR pulses used in bright-blood LGE and T1 mapping are typically non-selective adiabatic HS pulses with a narrow spectral bandwidth of around 1 kHz (Figure 3). In 2014, Rashid et al. [42] demonstrated that CIEDs can cause a frequency resonance offset of 2–6 kHz at a distance of 5–10 cm from the pulse generator, which is well outside the 1 kHz spectral bandwidth of a conventional
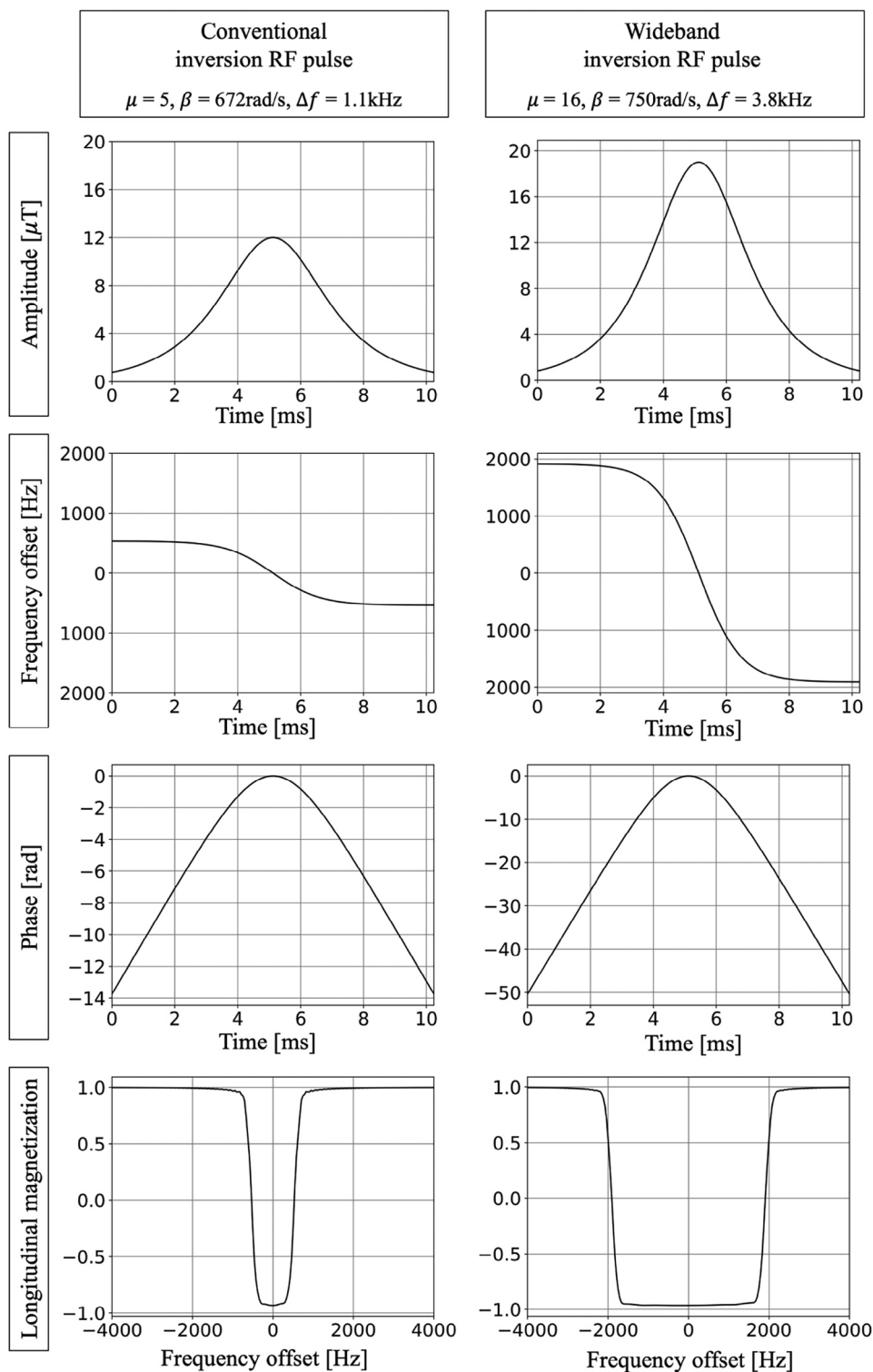
FIGURE 3 | Adiabatic hyperbolic secant radiofrequency (RF) pulse with corresponding amplitude modulation, frequency modulation, phase modulation, and longitudinal magnetization inversion profile. Left: conventional inversion pulse with a spectral bandwidth of 1.1 kHz. Right: wideband inversion pulse with a spectral bandwidth of 3.8 kHz.

IR or SR pulse. As a result, spins precessing outside the spectral bandwidth of the IR or SR pulses are not properly inverted or saturated, leading to spatial misregistration. This misregistration results in hyperintensity artifacts that obscure the myocardium and signal voids around the pulse generator.

5.1.2 | Technical Solution

To ensure correct inversion or saturation of the myocardial signal affected by the CIED, Rashid et al. [42] broadened the spectral bandwidth of the non-selective adiabatic HS IR pulse in the IR-LGE sequence from 1.1 kHz ($\beta = 672$ rad/s, $\mu = 5$), with a B1
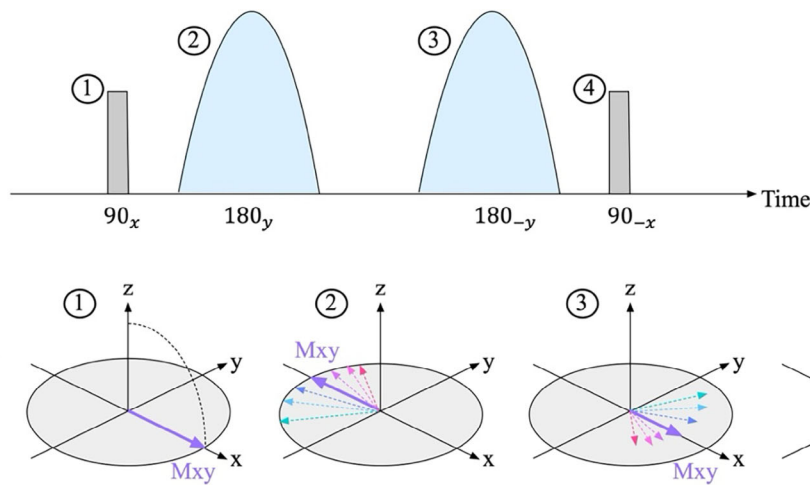
FIGURE 4 | Illustration of an adiabatic T2 preparation [50]. An initial 90° tip-down radiofrequency (RF) pulse is applied along the x-axis (transverse plane) to rotate the magnetization, followed by two refocusing RF pulses, each lasting 12.8 ms. A 90° tip-up RF pulse reverses the magnetization along the z-axis (longitudinal direction). After the T2 preparation module, a crusher gradient eliminates any residual transverse magnetization. Mo, initial longitudinal magnetization; Mxy, transverse magnetization; Mz, final longitudinal magnetization.

peak amplitude of 12 μT, to 3.8 kHz ($\beta = 750$ rad/s, $\mu = 16$), with a B1 peak amplitude of 19 μT, while maintaining the same pulse duration (Figure 3). This technique is known as wideband LGE. To further reduce hyperintensity artifacts, they also suggested applying a frequency shift pulse between −1.5 and 1.5 kHz to the IR.

5.2 | T2 preparation

5.2.1 | Technical Challenges

A T2 preparation module can be used in dark-blood imaging [47, 48] or mapping [49] sequences. A commonly used B1-insensitive adiabatic T2 preparation module introduced by Nezafat et al. [50] consists of a 90° tip-down pulse, of two adiabatic HS refocusing pulses, and of a 90° tip-up pulse (Figure 4). In 2024, Gut et al. [45] showed that using a this B1-insensitive adiabatic T2 preparation with a wideband IR in CIED patients resulted in severe CIED-related artifacts. Their HS refocusing pulse had a duration of 12.8 ms and a spectral bandwidth of 1.6 kHz.

5.2.2 | Technical Solution

In order to reduce CIED-related artifacts using a T2 preparation pulse, the spectral bandwidth of the HS refocusing pulses can be increased to 5 kHz ($\mu = 25$, $\beta = 785$ rad/s; originally created for a pulse duration of 10.24 ms, yielding a bandwidth of 6.2 kHz), while maintaining the same pulse duration of 12.8 ms and with a B1 peak amplitude of 30 μT.

5.3 | Excitation

5.3.1 | Technical Challenges

Compared to two-dimensional (2D) LGE, three-dimensional (3D) LGE reveals additional types of CIED-related artifacts using

selective slab excitation: extended signal void and banding artifacts [43]. The presence of CIEDs gives rise to spatially varying off-resonance effects that result in slab distortion. Consequently, spins near the ICD that are outside the excitation slab profile can be excited. As these regions may extend beyond the slice oversampling region, they wrap around in the image volume, producing foldover artifacts. Since slab distortion is inversely proportional to the slab selection gradient, to reduce slab distortion and associated ripple artifacts, the slab selection gradient needs to be increased. Therefore, both the RF excitation bandwidth and the slab oversampling factor must be increased [43].

5.3.2 | Technical Solution

Rashid et al. [43] suggested increasing the RF excitation bandwidth and the slab oversampling factor to enhance the slab selection gradient, thereby reducing associated ripple artifacts and extended signal void. In their study, the conventional RF excitation pulse was a sinc pulse with a duration of 600 μs, a bandwidth of 5.83 kHz, and a B1 amplitude of 7.57 μT. To mitigate artifacts, they proposed increasing the bandwidth-time product of the RF excitation pulse to achieve a bandwidth of 12 kHz while maintaining the same pulse duration, resulting in a new B1 amplitude of 15.66 μT.

6 | CMR in CIED Patients

In the following section, we will review the current clinical sequences used in patients with CIEDs, emphasizing wideband MRI techniques for LGE sequences. A summary of these wideband MRI protocols and adjustments, which aim to reduce CIED-related artifacts, is provided in Table 1.
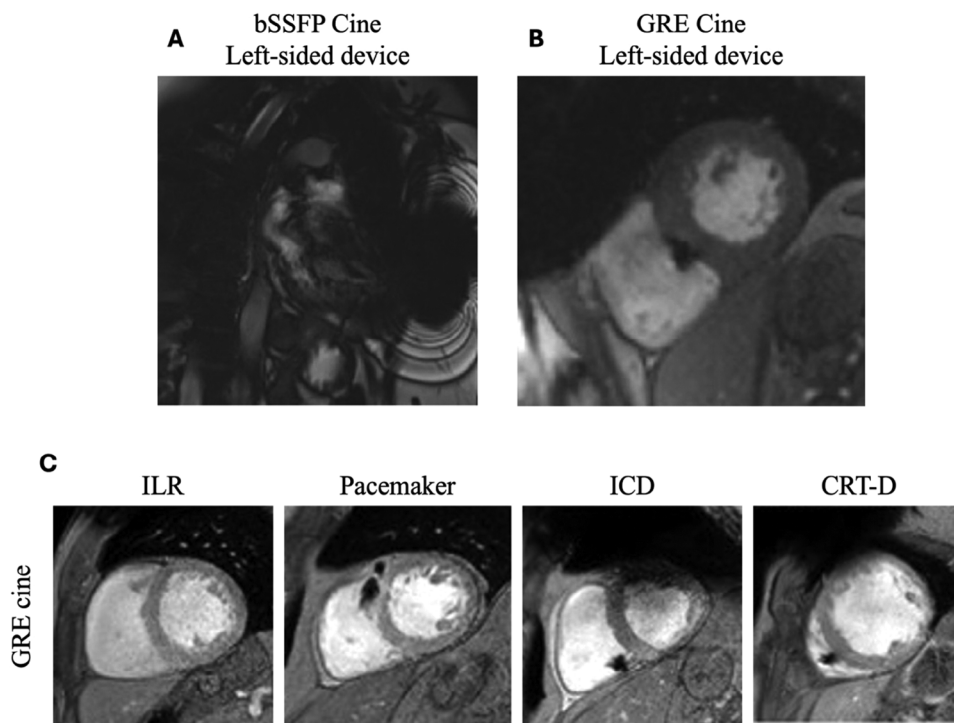
FIGURE 5 | Example of cine imaging with CIED. (A) bSSFP cine imaging with a left-sided device is strongly degraded by CIED-related banding artifacts. (B) GRE cine imaging with a left-sided device is not degraded by CIED-related artifacts. (C) GRE cine imaging with left-sided ILR, pacemaker, ICD, CRT-D. ICD and CRT are the most artifacted by CIED. bSSFP, balanced steady-state free-precession; CIED, cardiac implantable electronic device; CRT-D, cardiac resynchronization therapy; GRE, gradient recalled echo; ICD, implantable cardioverter defibrillator; ILR, implantable loop recorders. (A) and (B) adapted from Raphael et al. [58]. (C) adapted from Lobe et al. [60].

6.1 | Functional Assessment With Cine

Cardiac cine imaging is essential for assessing cardiac ventricular function, as it allows dynamic visualization of heart anatomy and wall motion [51, 52]. The steady-state bSSFP cine sequence [53] is a widely used sequence for evaluating ventricular volume, myocardial mass, ejection fraction, and wall motion due to its high SNR, excellent blood-myocardium contrast, and short acquisition times. However, bSSFP is sensitive to off-resonance frequencies, causing banding artifacts, problematic in patients with CIEDs [54]. This sensitivity is influenced by the repetition time (TR), with longer TRs inducing artifacts even far from the device. Strategies to reduce TR include asymmetrical and partial Fourier readouts, parallel imaging, and increased receiver bandwidth. Alternatively, using a GRE readout can eliminate the TR dependency of bSSFP on metal artifacts, with further reduction in sensitivity achieved by minimizing echo time through partial Fourier readout, parallel imaging, asymmetrical echo, and higher receiver bandwidth [55, 56]. The 2024 SCMR consensus [24] recommends cine imaging in CIED patients with short RF pulses (<1 ms), low flip angles (10°–15°), high receiver bandwidth (>500 Hz), and GRE readouts to avoid banding artifacts.

Several studies have compared cine bSSFP and cine GRE in CIED patients. In 2011, Sasaki et al. [57] showed that bSSFP cine at 1.5 T resulted in severe banding artifacts, especially in patients with left-sided ICDs, with artifact size correlating with the generator size. In 2015, Raphael et al. [58] found cine bSSFP to be non-diagnostic in pacemaker patients, while cine GRE eliminated artifacts (Figure 5). Similarly, Hilbert et al. [59], Löbe et al. [60], and Barison et al. [61] demonstrated that cine bSSFP at 1.5 T was more pronte to artifacts, particularly in patients with ICDs and CRT-Ds, with cine GRE significantly improving image quality, especially post-contrast (Figure 5). Holtstiege et al. [62] further showed that cine GRE enabled accurate assessment in 74% of S-ICD patients.

6.2 | Myocardial Viability Assessment With LGE

Bright-blood LGE MRI is the clinical gold standard for assessing myocardial scars and viability [38, 63, 64]. This technique uses an IR pulse to darken healthy myocardium while enhancing the visibility of scar tissue, making it susceptible to CIED-associated hyperintensity artifacts in the myocardium due to improper inversion of the magnetization.

6.2.1 | 2D wideband LGE at 1.5 T

In 2014, Rashid et al. [42] were the first to apply wideband IR GRE (3.8 kHz) in CMR, imaging 12 ICD patients with known left ventricular scarring. This approach fully resolved hyperintensity artifacts in the myocardium, enabling comprehensive scar assessment (Figure 6). This study marked a milestone in CMR with CIEDs, subsequently leading to numerous clinical studies using 2D wideband IR LGE. Later, the same group conducted a two-center study involving 25 CIED patients, showing that
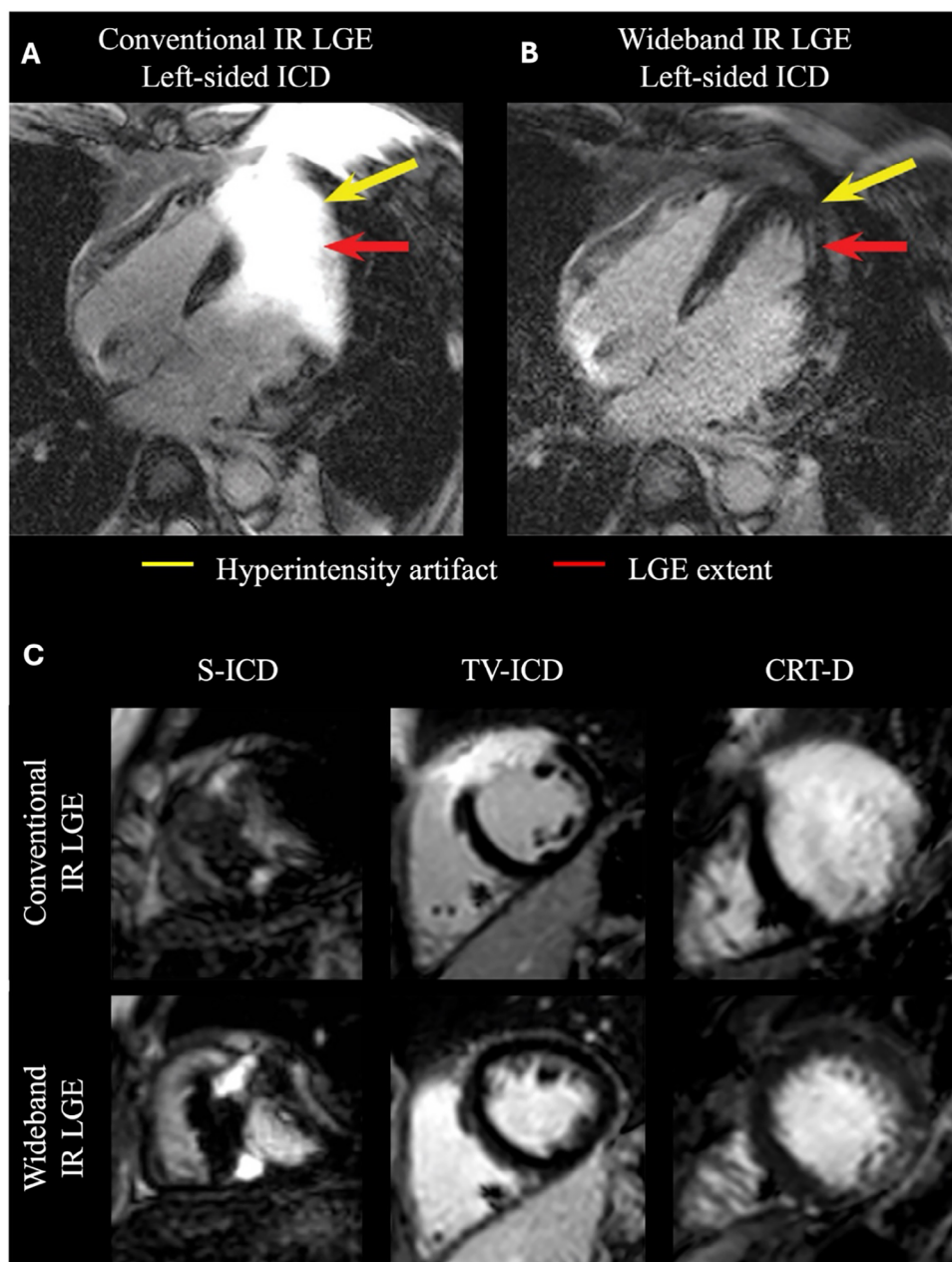
FIGURE 6 | Example of GRE IR LGE imaging with CIED. (A) Conventional IR (1.1 kHz) LGE in a patient with a left-sided ICD, with an IR pulse bandwidth of 1.1 kHz. Severe hyperintensity artifacts (yellow) obscure the extent of the LGE (red) and hamper detection and diagnosis of the myocardial lesion. (B) Wideband IR (3.8 kHz) LGE in the same patient, with an IR pulse bandwidth of 3.8 kHz. No artifact obscures the myocardium and the extent of the LGE can be detected. (C) Conventional and wideband IR LGE with S-ICD, TV-ICD, and CRT-D. With wideband IR, hyperintensity artifacts are successfully suppressed in the presence of TV-ICD and CRT-D, but residual artifacts still obscure the myocardium in the presence of S-ICD. CIED, cardiac implantable electronic device; CRT-D, cardiac resynchronization therapy; GRE, gradient recalled echo; ICD, implantable cardioverter defibrillator; IR, inversion recover; LGE, late gadolinium enhancement; S-ICD, subcutaneous implantable cardioverter defibrillator; TV-ICD, transvenous implantable cardioverter defibrillator. (A) and (B) adapted from Rashid et al. [42]. (C) adapted from Singh et al. [35].

while conventional applied IR (1.1 kHz) caused severe artifacts in ICD patients, wideband IR (3.8 kHz) successfully suppressed these artifacts [65]. Singh et al. [66] confirmed that wideband IR GRE can resolve CIED-related artifacts in TV-ICDs and CRT-Ds, though residual artifacts may remain with S-ICDs (Figure 6). In 2014, Stevens et al. [33] correlated wideband IR LGE (3.8 kHz) with electroanatomical mapping (EAM) in patients referred for ventricular tachycardia (VT) ablation, finding strong concordance between the two methods in scar detection (Figure 7). In

2019, Singh et al. [66] applied wideband IR LGE (3.8 kHz) in 49 ICD patients with VT or heart failure, eliminating artifacts in 61% of cases, particularly in TV-ICD patients. Additionally, similar to Stevens et al. [33], they compared the scars identified by wideband LGE in 27 patients undergoing VT ablation with invasive EAM. They demonstrated a strong correlation between wideband LGE and EAM in 78% of patients. Bhuva et al. [67], also in 2019, evaluated wideband IR LGE (3.8 kHz) in 136 CIED patients (22% ILRs, 40% pacemakers, 38% ICDs), including
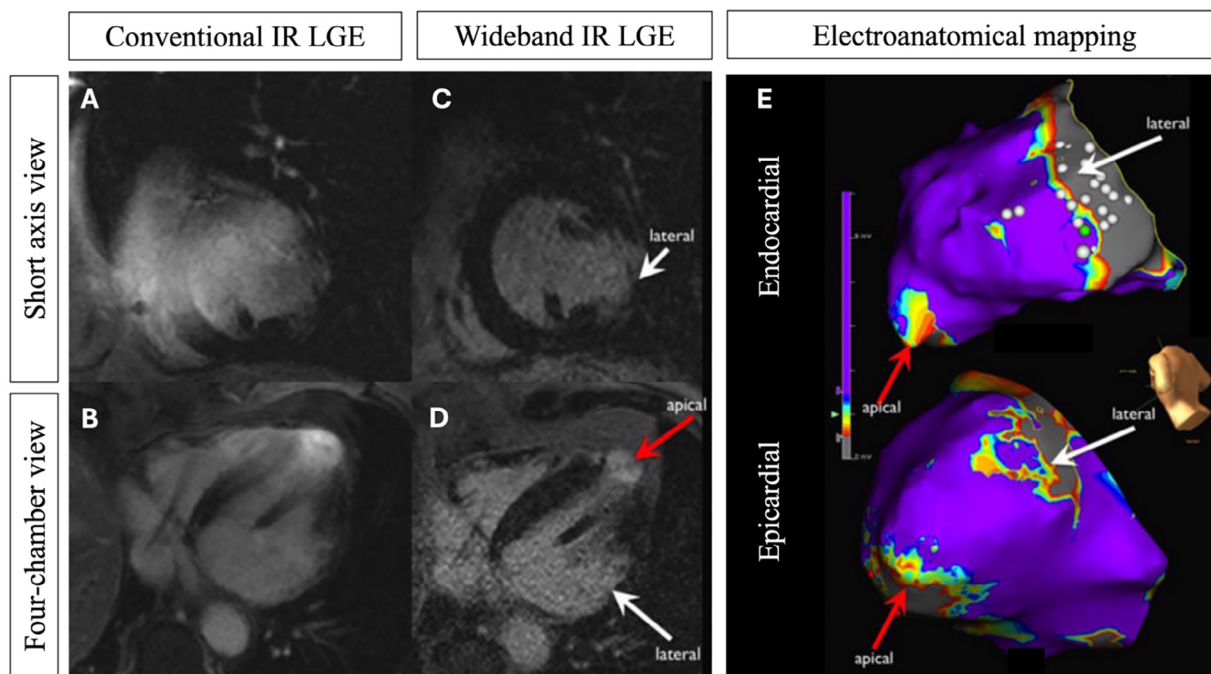
FIGURE 7 │ Comparison of GRE IR LGE imaging to electroanatomical mapping in a patient with a left-sided implantable cardioverter defibrillator. Conventional IR (1.1 kHz) LGE results in hyperintensity artifacts obscuring the myocardium on the short-axis (A) and four-chamber (B) views. Wideband IR (3.8 kHz) LGE suppresses ICD-related artifacts revealing myocardial lesions in the apex and basal lateral segment, correlating with electroanatomical mapping. IR, inversion recovery; LGE, late gadolinium enhancement. Figure adapted from Stevens et al. [33].

42% with non-MRI-conditional CIEDs. They found that 43% of patients had non-diagnostic results with conventional LGE (79% of ICDs), compared to 0% with wideband LGE, which detected all myocardial scars and led to clinical management changes in 83% of cases. The study's impact was most notable in procedural planning for VT ablation and diagnosing myocardial infarction and cardiomyopathies, particularly in patients with non-MRI-conditional devices. In 2022, Patel et al. [68] assessed 179 CIED patients who were referred for VT substrate evaluation and found wideband LGE (3.8 kHz) altered diagnosis in 36% of cases, particularly in those referred for VT or cardiomyopathy evaluation, and impacted clinical management in 28% of patients, influencing decisions on revascularization, medications, and VT planning ablation.

6.2.2 │ 2D Wideband LGE at 3 T

Although many studies using 2D wideband LGE have been published at 1.5 T, only one study using wideband LGE at 3 T has been found. In 2015, Ranjan et al. [69] investigated, for the first time, the feasibility of wideband LGE (3.8 kHz) at 3 T to extend the availability of wideband LGE MRI to all clinical MRI settings and to enable higher spatial resolution for better detection of border zones. To reduce CIED-induced artifacts, they increased the spectral bandwidth of the IR pulse from 1 kHz ($\beta = 672$ rad/s, $\mu = 5$, IR duration = 10.2 ms) to 3.8 kHz ($\beta = 750$ rad/s, $\mu = 10$, IR duration = 6.1 ms). In an animal experiment with seven canines with scars in the right and left ventricles, they validated the wideband LGE sequence with an ICD taped to the left shoulder, approximately 10 cm away from the heart. The wideband LGE MRI resulted in no significant

ICD-related artifacts and was consistent with gross pathology (histology). Additionally, they were able to map the scar in 3D from a stack of 2D artifact-free short-axis wideband LGE images with an ICD and compare it to 3D LGE without an ICD. They found that wideband LGE with an ICD showed 93% agreement with 3D LGE without an ICD. It was concluded that wideband LGE MRI enables accurate detection of myocardial scars at 3 T.

6.2.3 │ 3D Wideband LGE at 1.5 T

Although 2D LGE is effective for detecting myocardial fibrosis, infarction [70, 71], and various nonischemic cardiomyopathies [72], it faces challenges due to its low spatial resolution and partial volume effects [73]. Free-breathing 3D high-resolution LGE sequences overcome these challenges, providing whole-heart coverage and improving the detection of small scars that might otherwise be invisible and guiding ablation procedures [21]. In patients with VT, 3D LGE can identify scar and border zones, which can be integrated with EAM to guide ablation. However, most patients referred for VT ablation procedures have ICDs, which pose artifact challenges [74]. In 2016, Rashid et al. [43] applied 3D wideband LGE at 1.5 T using wideband IR (3.8 kHz) and wideband excitation RF pulses (12 kHz) in six volunteers and five VT patients with ICDs. With a respiratory-gating, $1.4 \times 1.4 \times 4.0$ mm^3 resolution and Cartesian sampling, they showed that wideband IR and wideband excitation RF pulses substantially reduced ICD-related artifacts. In 2024, Hong et al. [75] used wideband 3D LGE with isotropic resolution (1.5–2 mm^3) in 16 ICD patients. To address long acquisition times, they employed stack-of-stars sampling with XD-GRASP reconstruction and 2D

self-navigation for motion correction. The 3D wideband LGE significantly reduced artifacts, allowing clear visualization of arrhythmogenic substrates. They also demonstrated good agreement between 3D LGE gray zones and VT ablation points in one patient, highlighting its potential to enhance ablation planning.

6.2.4 | 2D Black-Blood LGE at 1.5 T

Although bright-blood LGE provides excellent contrast between healthy and injured myocardium, it still suffers from poor contrast at the scar-blood interface, giving raise to ambiguity in image interpretation and making it particularly challenging to depict small and subendocardial scars. Dark-blood LGE imaging [47, 48] has been developed to improve scar-to-blood contrast by combining magnetization preparation, such as T2 preparation, with IR, which simultaneously darkens blood and healthy myocardium signals while enhancing scar tissue visibility.

In 2024, Gut et al. [45] introduced wideband black-blood LGE imaging at 1.5 T to improve scar-to-blood contrast combining T2 preparation with IR in CIED patients. The authors used a wideband IR (3.8 kHz) pulse and T2 preparation with wideband refocusing pulses (5.0 kHz). Their study included six CIED patients (pacemakers, ICDs) and one sheep. The wideband black-blood LGE technique successfully suppressed CIED-induced hyperintensity artifacts in the myocardium, improving scar-to-blood contrast and allowing better scar detection compared to conventional bright-blood LGE (Figure 8). They also performed histological analysis in the animal to compare tissue fibrosis detection with black-blood LGE, finding that the myocardial scars detected with wideband black-blood LGE corresponded well with the scars localized through histology.

6.3 | Guidance for VT Ablation

CMR LGE is utilized not only for diagnosis but also to guide ablation procedures, as it facilitates scar mapping and ablation. LGE enables precise identification and characterization of the arrhythmogenic substrate, allowing for the depiction of slow-conducting channels (CCs) between the scar and the viable myocardium, which are often the origin of scar-related VT. This has a high correlation with EAMs [76–78]. However, most patients requiring VT ablation have an ICD, which can cause hyperintensity artifacts that complicate ablation planning. In 2020, Roca-Luque et al. [79] used 2D wideband LGE at 1.5 T with an IR of 3.8 kHz to assess its feasibility and accuracy in identifying CC entrances to guide VT ablation in ICD patients. They compared the number and location of CC entrances identified with wideband LGE to those identified with 3D EAM. Their study demonstrated that wideband LGE was as accurate as EAM in identifying CC entrances in ICD patients and was as accurate as conventional LGE in patients without ICDs compared to EAM. This establishes wideband LGE as a valid sequence for identifying CCs and planning VT ablations.

## 6.4 | Myocardial Tissue Characterization

6.4.1 | 2D T1 Mapping at 1.5 T

Parametric mapping enables the visualization and quantification of changes in myocardial tissue composition. T1 mapping is considered the gold standard for characterizing both focal and diffuse fibrosis. Conventional T1 mapping techniques, such as modified Look-Locker inversion recovery (MOLLI) or SASHA, use IR or SR pulses at various recovery times. However, these sequences are limited by off-resonance artifacts in CIED patients due to the use of IR or SR pulses. Additionally, T1 mapping often employs a bSSFP readout, which is further restricted by banding artifacts.

In 2015, Hong et al. [80] developed a wideband arrhythmia-insensitive rapid (AIR) SR sequence for T1 mapping at 1.5 T, specifically for CIED patients (Figure 9). The SR pulse consisted of a BISTRO RF pulse train (15 HS IR pulses, 3.07 ms each) to fully rotate longitudinal magnetization into the transverse plane. Crusher and spoiler gradients minimized stimulated echoes and dephased residual transverse magnetization. The sequence incorporated a wideband SR pulse (8.9 kHz) and GRE readout to achieve uniform T1 weighting in the presence of ICDs. Despite low SNR and resolution, the wideband AIR sequence enabled T1 mapping without significant ICD-induced artifacts at 1.5 T. In 2017, Shao et al. [44] introduced a wideband fast low angle shot (FLASH) MOLLI sequence for T1 mapping using wideband IR (3.8 kHz) in CIED patients at 1.5 T (Figure 10). They employed a M0-(1)-5-(1)-3-(1)-1 scheme with wideband IR pulses and shortest TI values of 100, 180, and 260 ms, with a dummy heartbeat between each inversion. In phantom studies, T1 values with and without ICD showed a maximum error of 3%. In a volunteer study, T1 values obtained with wideband FLASH MOLLI with and without an ICD showed no significant difference. Finally, in volunteers and 10 ICD patients, wideband FLASH MOLLI was compared to wideband bSSFP MOLLI. Severe ripple artifacts were observed in the myocardium with wideband bSSFP MOLLI, whereas wideband FLASH MOLLI showed no or negligible artifacts.

6.5 | Myocardial Perfusion Imaging

Myocardial perfusion imaging, or stress perfusion, evaluates blood flow through the heart muscle in patients with known or suspected coronary artery disease, employing gadolinium-based contrast agents [81–83]. In CMR perfusion, areas of reduced signal intensity indicate perfusion abnormalities related to infarction or ischemia. Studies on CMR perfusion in patients with MR-conditional [84, 85] and non-conditional devices [86] have shown good diagnostic image quality in MR-conditional patients but noted non-diagnostic image quality in those with non-conditional devices due to hyperintensity artifacts. In 2018, Hong et al. [87] introduced a wideband perfusion imaging sequence with a wideband SR pulse [80] using a BISTRO pulse train consisting of three wideband HS IR pulses (9.2 kHz). In 16 CIED patients, they found that 18% of myocardial segments had severe hyperintensity artifacts with standard perfusion, compared to only 3% with wideband perfusion (Figure 11). In 2020, the same group developed an accelerated wideband perfusion sequence using compressed
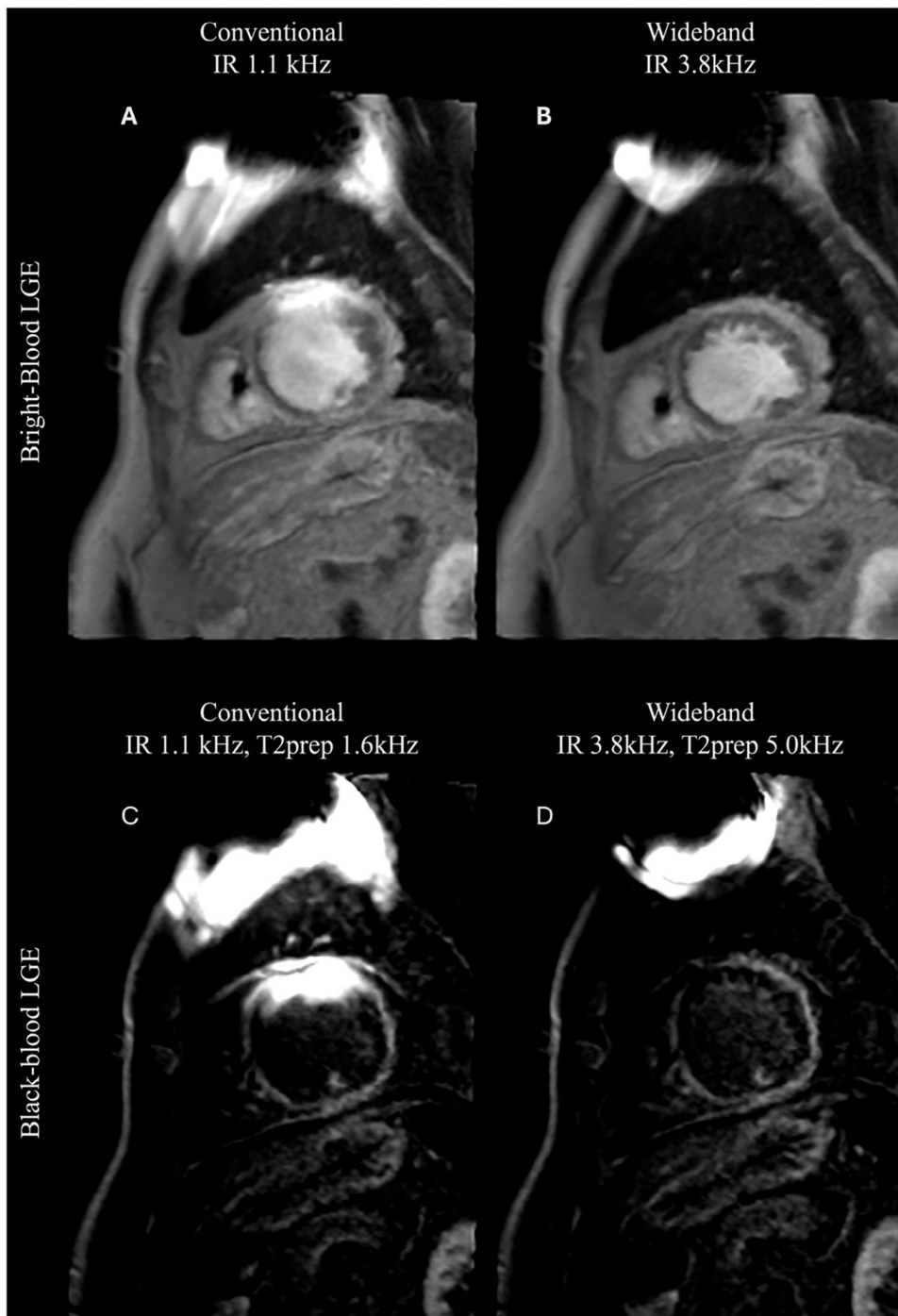
FIGURE 8 | Example of GRE bright-blood IR LGE and GRE black-blood IR-T2prep LGE in a patient with a left-sided ICD. (A) Conventional bright-blood IR (1.1 kHz) LGE with hyperintensity artifacts obscuring the myocardium. (B) Wideband bright-blood IR (3.8 kHz) LGE with artifacts suppressed. The poor scar-to-blood contrast challenges the detection of the extent of LGE. (C) Conventional black-blood IR-T2prep (0.8–1.6 kHz) LGE with hyperintensity artifacts obscuring the myocardium. (D) Wideband black-blood IR-T2prep (3.8–5.0 kHz) LGE with suppressed artifacts. The improved scar-to-blood contrast enables the detection of LGE extent in all segments. GRE, gradient recalled echo; ICD, implantable cardioverter defibrillator; IR, inversion recover; LGE, late gadolinium enhancement. Figure adapted from Gut et al. [45].

sensing reconstruction [88]. With five-fold accelerated lattice-like Cartesian sampling, resting perfusion scans in 10 CIED and 10 non-CIED patients showed diagnostically acceptable image quality and reliable myocardial blood flow quantification in all CIED patients, with no significant differences in median resting blood flow between patients with and without CIEDs.

7 | Conclusion

CMR imaging in patients with CIEDs can be safely performed at 1.5 T with both MR-conditional and non-conditional cardiac implants when strict protocols are followed. However, a significant challenge remains: image artifacts resulting from the
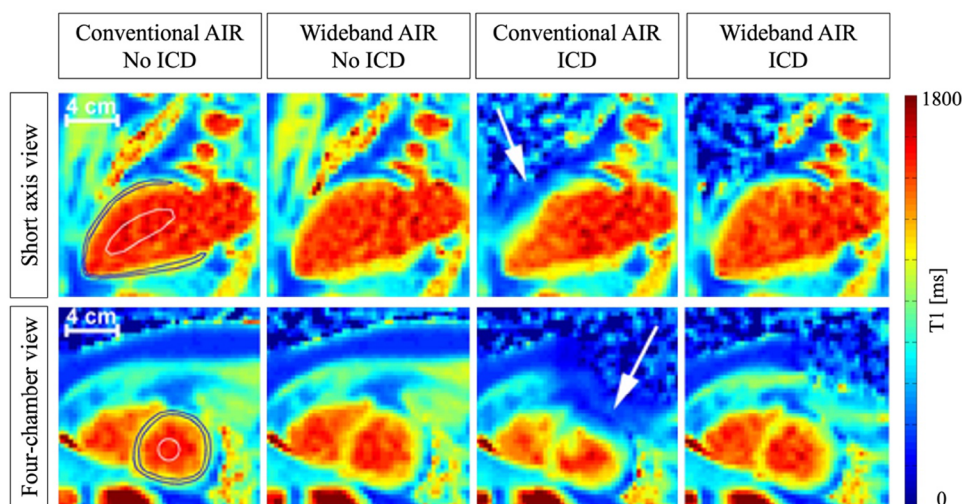
FIGURE 9 | Conventional and wideband AIR T1 mapping in a volunteer with and without an ICD taped on the left shoulder 10 cm from the heart. Wideband AIR T1 mapping with a wideband saturation pulse with a bandwidth of 8.9 kHz produced accurate T1 values in the presence of an ICD, close to those obtained with conventional AIR without an ICD (control), both in the short-axis and in the four-chamber views. AIR, arrhythmia-insensitive rapid; ICD, implantable cardioverter defibrillator. Figure adapted from Kim and coworkers [80].
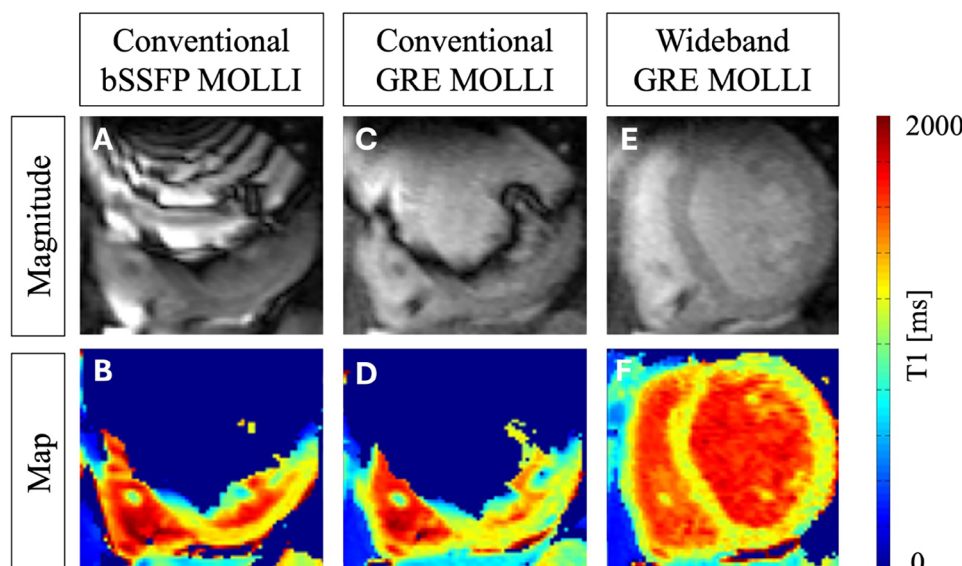
FIGURE 10 | Example of MOLLI T1 mapping in an ICD patient. Conventional bSSFP MOLLI T1 mapping resulted in severe ICD-related banding artifacts in the magnitude image (A), giving inaccurate T1 values in the T1 map (B). Conventional GRE MOLLI T1 mapping also resulted in ICD-related banding artifacts in the magnitude image (C), giving inaccurate T1 values in the T1 map (D). GRE wideband MOLLI T1 mapping with a 3.8 kHz bandwidth wideband inversion pulse removed ICD-related artifacts in the magnitude image (E), providing correct T1 values in the T1 map (F). bSSFP, balanced steady-state free-precession; GRE, gradient recalled echo; ICD, implantable cardioverter defibrillator; MOLLI, modified Look-Locker inversion-recovery. Figure adapted from Shao et al. [44].

interaction between the magnetic components of CIEDs and the MRI environment. Severe hyperintensity, signal void, and banding artifacts can obscure the myocardium, complicating diagnosis and patient management. In this review, we first introduced the potential adverse effects of CMR with CIEDs and the interactions between CIEDs and the MRI environment. Next, we described the technical advancements in wideband MRI that help suppress CIED-related artifacts. Finally, we summarized the various clinical applications of wideband MRI in CMR.

Wideband solutions with GRE have been widely applied and validated for bright-blood LGE in 2D imaging. However, only a few studies have explored wideband techniques for 3D LGE, 2D T1 mapping, and 2D perfusion. Further research is warranted for applications in low-field (0.55 T) and higher field (3 T) MRI. Furthermore, to date no wideband studies have been conducted for extracellular volume imaging or 2D/3D T1ρ, T2, and T2* mapping, and CMR angiography in CIED patients. Implementing CMR protocols that include wideband LGE and wideband T1ρ, T2, T2*, and ECV mapping in the presence of CIEDs could transform both
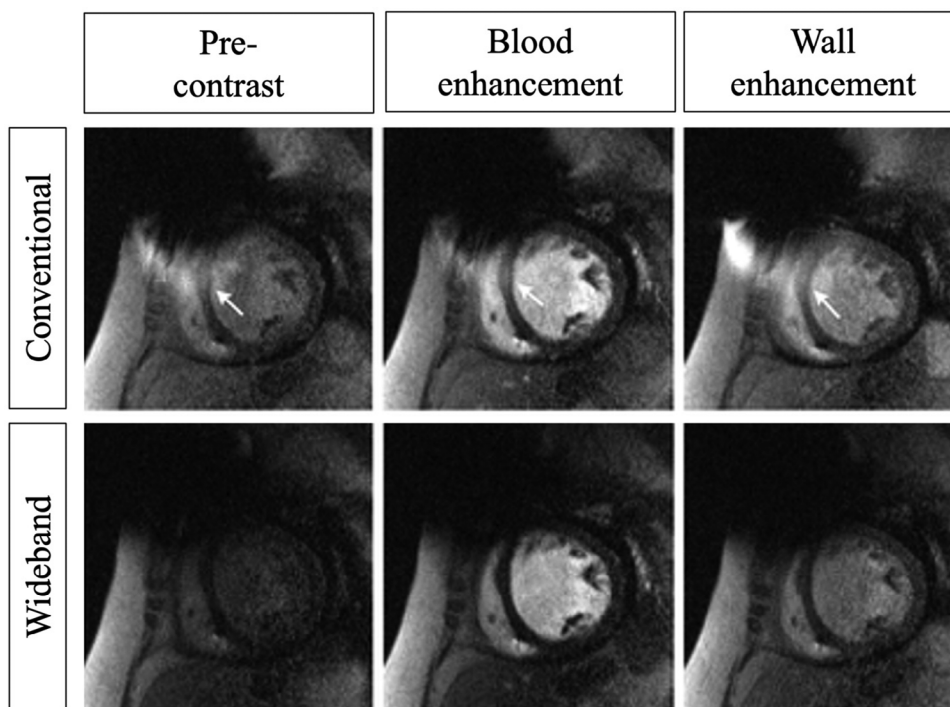
FIGURE 11 | Example of conventional and wideband perfusion in a patient with an implantable cardioverter defibrillator (ICD) after gadolinium injection. ICD-related hyperintensity artifacts obscured the myocardium pre-contrast, at peak blood enhancement, and at peak wall enhancement, using a conventional perfusion sequence with a saturation pulse with a 2.5 kHz bandwidth, but were suppressed using a wideband perfusion sequence with a saturation pulse with a 9.2 kHz bandwidth. Figure adapted from Hong et al. [87].
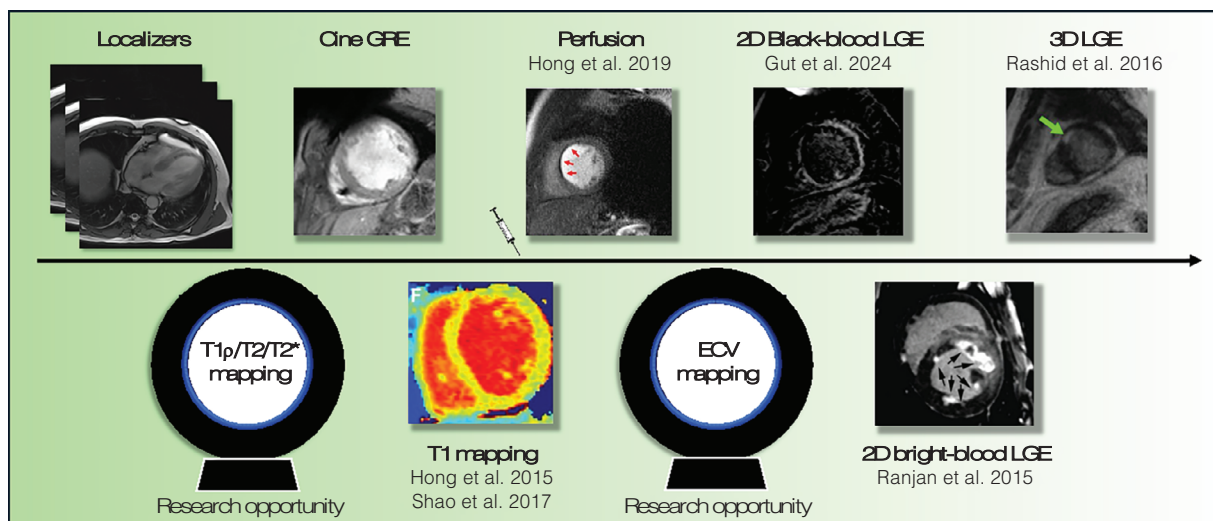
FIGURE 12 | Typical cardiac magnetic resonance imaging protocol for patients with cardiac implantable electronic devices: available sequences and future research opportunities. ECV, extracellular volume; GRE, gradient recalled echo; LGE, late gadolinium enhancement.

research and clinical practice (Figure 12). These advancements would provide clinicians with sophisticated tools for accurate diagnosis, treatment planning, and prognostic assessment, ultimately leading to improved patient outcomes and enhanced healthcare delivery. The role of wideband solutions in CMR with CIEDs is expected to expand, driving innovation and change in cardiovascular medicine. Additionally, incorporating AI-based image processing for artifact correction and segmentation [89] in CMR with CIEDs holds significant clinical promise for advancing

patient care, automating post-processing tasks, and improving diagnostic precision and outcomes [90].

and from the European Research Council (ERC) under the European Union's Horizon 2020 research and innovation program (grant agreement 101076351) for the support.

Ethics Statement

The authors have nothing to report.

Conflicts of Interest

The authors declare no conflicts of interest.

Data Availability Statement

Data sharing is not applicable to this article as no new data were created or analyzed in this study.

References

1. V. R. Vaidya, R. Asirvatham, G. N. Kowlgi, et al., "Trends in Cardiovascular Implantable Electronic Device Insertion Between 1988 and 2018 in Olmsted County," *JACC: Clinical Electrophysiology* 8 (2022): 88–100.

2. N. J. Patel, S. Edla, A. Deshmukh, et al., "Gender, Racial, and Health Insurance Differences in the Trend of Implantable Cardioverter-Defibrillator (ICD) Utilization: A United States Experience over the Last Decade," *Clinical Cardiology* 39 (2016): 63–71.

3. F. M. Kusumoto, M. H. Schoenfeld, B. L. Wilkoff, et al., "2017 HRS Expert Consensus Statement on Cardiovascular Implantable Electronic Device Lead Management and Extraction," *Heart Rhythm* 14 (2017): e503–e551.

4. S. G. Priori, C. Blomstrom-Lundqvist, A. Mazzanti, et al., "2015 ESC Guidelines for the Management of Patients With Ventricular Arrhythmias and the Prevention of Sudden Cardiac Death: The Task Force for the Management of Patients With Ventricular Arrhythmias and the Prevention of Sudden Cardiac Death of the European Society of Cardiology (ESC)," *European Heart Journal* 36 (2015): 2793–2867l.

5. P. Ponikowski, A. A. Voors, S. D. Anker, et al., "2016 ESC Guidelines for the Diagnosis and Treatment of Acute and Chronic Heart Failure: The Task Force for the Diagnosis and Treatment of Acute and Chronic Heart Failure of the European Society of Cardiology (ESC)," *European Heart Journal* 37 (2016): 2129–2200.

6. G. Boriani and M Vitolo. "Infection of Cardiac Implantable Electrical Devices: An Emerging Epidemiological Issue," in *Infections of Cardiac Implantable Devices: A Comprehensive Guide*, eds. I Diemberger and G Boriani (Springer, 2020), 1–16.

7. R. Kalin and M. S. Stanton, "Current Clinical Issues for MRI Scanning of Pacemaker and Defibrillator Patients," *Pacing and Clinical Electrophysiology* 28 (2005): 326–328.

8. A. Roguin, M. M. Zviman, G. R. Meininger, et al., "Modern Pacemaker and Implantable Cardioverter/Defibrillator Systems Can be Magnetic Resonance Imaging Safe: In Vitro and in Vivo Assessment of Safety and Function at 1.5 T," *Circulation* 110 (2004): 475–482.

9. S. Nazarian and H. R. Halperin, "How to Perform Magnetic Resonance Imaging on Patients With Implantable Cardiac Arrhythmia Devices," *Heart Rhythm* 6 (2009): 138–143.

10. S. Nazarian, R. Hansford, A. Roguin, et al., "A Prospective Evaluation of a Protocol for Magnetic Resonance Imaging of Patients with Implanted Cardiac Devices," *Annals of Internal Medicine* 155 (2011): 415.

11. S. Nazarian, A. Roguin, M. M. Zviman, et al., "Clinical Utility and Safety of a Protocol for Noncardiac and Cardiac Magnetic Resonance Imaging of Patients with Permanent Pacemakers and Implantable-Cardioverter Defibrillators at 1.5 Tesla," *Circulation* 114 (2006): 1277.

12. J. D. Cohen, H. S. Costa, and R. J. Russo, "Determining the Risks of Magnetic Resonance Imaging at 1.5 Tesla for Patients With Pacemakers and Implantable Cardioverter Defibrillators," *American Journal of Cardiology* 110 (2012): 1631–1636.

13. S. Nazarian, R. Hansford, A. A. Rahsepar, et al., "Safety of Magnetic Resonance Imaging in Patients With Cardiac Devices," *New England Journal of Medicine* 377 (2017): 2555–2564.

14. A. D. Shah, M. A. Morris, D. S. Hirsh, et al., "Magnetic Resonance Imaging Safety in Nonconditional Pacemaker and Defibrillator Recipients: A Meta-Analysis and Systematic Review," *Heart Rhythm* 15 (2018): 1001–1008.

15. G. N. Levine, A. S. Gomes, A. E. Arai, et al., "Safety of Magnetic Resonance Imaging in Patients With Cardiovascular Devices: An American Heart Association Scientific Statement From the Committee on Diagnostic and Interventional Cardiac Catheterization, Council on Clinical Cardiology, and the Council on Cardiovascular Radiology and Intervention," *Circulation* 26 (2007): 2878–2891.

16. J. H. Indik, J. Rod Gimbel, H. Abe, et al., "2017 HRS Expert Consensus Statement on Magnetic Resonance Imaging and Radiation Exposure in Patients With Cardiovascular Implantable Electronic Devices," *Heart Rhythm* 14 (2017): 97–153.

17. K. K. Vigen, S. B. Reeder, M. N. Hood, et al., "Recommendations for Imaging Patients with Cardiac Implantable Electronic Devices (CIEDs)," *Journal of Magnetic Resonance Imaging* 53 (2021): 1311–1317.

18. A. Roguin, J. Schwitter, C. Vahlhaus, et al., "Magnetic Resonance Imaging in Individuals With Cardiovascular Implantable Electronic Devices," *Europace* 10 (2008): 336–346.

19. A. Roguin, J. K. Donahue, C. S. Bomma, D. A. Bluemke, and H. R. Halperin, "Cardiac Magnetic Resonance Imaging in a Patient With Implantable Cardioverter-Defibrillator," *PACE—Pacing and Clinical Electrophysiology* 28 (2005): 336–338.

20. T. Sasaki, R. Hansford, M. M. Zviman, et al., "Quantitative Assessment of Artifacts on Cardiac Magnetic Resonance Imaging of Patients With Pacemakers and Implantable Cardioverter Defibrillators," *Circulation: Cardiovascular Imaging* 4 (2011): 662.

21. T. Dickfeld, J. Tian, G. Ahmad, et al., "MRI-Guided Ventricular Tachycardia Ablation Integration of Late Gadolinium-Enhanced 3D Scar in Patients With Implantable Cardioverter-Defibrillators," *Circulation: Arrhythmia and Electrophysiology* 4 (2011): 172–184.

22. ASTM F2503–05, *Standard Practice for Marking Medical Devices and Other Items for Safety in the Magnetic Resonance Environment* (West Conshohocken, PA: ASTM International, 2005).

23. T. Sommer, C. P. Naehle, A. Yang, et al., "Strategy for Safe Performance of Extrathoracic Magnetic Resonance Imaging at 1.5 Tesla in the Presence of Cardiac Pacemakers in Non-Pacemaker-Dependent Patients: A Prospective Study With 115 Examinations," *Circulation* 114 (2006): 1285–1292.

24. D. Kim, J. D. Collins, J. A. White, et al., "SCMR Expert Consensus Statement for Cardiovascular Magnetic Resonance of Patients With a Cardiac Implantable Electronic Device," *Journal of Cardiovascular Magnetic Resonance* 26 (2024): 100995.

25. J. H. Indik, J. R. Gimbel, H. Abe, et al., "2017 HRS Expert Consensus Statement on Magnetic Resonance Imaging and Radiation Exposure in Patients With Cardiovascular Implantable Electronic Devices," *Heart Rhythm* 14 (2017): e97–e153.

26. E. Yang, M. Suzuki, S. Nazarian, and H. R. Halperin, "Magnetic Resonance Imaging Safety in Patients With Cardiac Implantable Electronic Devices," *Trends in Cardiovascular Medicine* 32 (2022): 440–447.

27. D. A. Langman, I. B. Goldberg, J. P. Finn, and D. B. Ennis, "Pacemaker Lead Tip Heating in Abandoned and Pacemaker-Attached Leads at 1.5 Tesla MRI," *Journal of Magnetic Resonance Imaging* 33 (2011): 426–431.

28. P. F. J. New, B. R. Rosen, T. J. Brady, et al., "Potential Hazards and Artifacts of Ferromagnetic and Nonferromagnetic Surgical and Dental Materials and Devices in Nuclear Magnetic Resonance Imaging," *Radiology* 147 (1983): 139–148.

29. W. Irnich, "Risks to Pacemaker Patients Undergoing Magnetic Resonance Imaging Examinations," *EP Europace* 12 (2010): 918–920.

30. I. Khodarahmi, A. Isaac, E. K. Fishman, D. Dalili, and J. Fritz, "Metal About the Hip and Artifact Reduction Techniques: From Basic Concepts to Advanced Imaging," *Seminars in Musculoskeletal Radiology* 23 (2019): E68–E81.

31. E. M. Lee, E. S. H. Ibrahim, N. D. Bs, et al., "Improving MR Image Quality in Patients With Metallic Implants," *Radiographics* 41 (2021): E126–E137.

32. T. Sasaki, R. Hansford, M. M. Zviman, et al., "Quantitative Assessment of Artifacts on Cardiac Magnetic Resonance Imaging of Patients With Pacemakers and Implantable Cardioverter-Defibrillators," *Circulation: Cardiovascular Imaging* 4 (2011): 662–670.

33. S. M. Stevens, R. Tung, S. Rashid, et al., "Device Artifact Reduction for Magnetic Resonance Imaging of Patients With Implantable Cardioverter-Defibrillators and Ventricular Tachycardia: Late Gadolinium Enhancement Correlation With Electroanatomic Mapping," *Heart Rhythm* 11 (2014): 289–298.

34. F. Del Grande, F. Santini, D. A. Herzka, et al., "Fat-Suppression Techniques for 3-T MR Imaging of the Musculoskeletal System," *Radiographics* 34 (2014): 217–233.

35. A. Singh, W. Chen, H. N. Patel, et al., "Impact of Wideband Late Gadolinium Enhancement Cardiac Magnetic Resonance Imaging on Device-Related Artifacts in Different Implantable Cardioverter-Defibrillator Types," *Journal of Magnetic Resonance Imaging* 54 (2021): 1257–1265.

36. C. Germann, D. Nanz, and R. Sutter, "Magnetic Resonance Imaging around Metal at 1.5 Tesla Techniques from Basic to Advanced and Clinical Impact," *Investigative Radiology* 56 (2021): 734–748.

37. A.-M. Vuorinen, L. Lehmonen, J. Karvonen, M. Holmström, S. Kivistö, and T. Kaasalainen, "Reducing Cardiac Implantable Electronic Device-Induced Artefacts in Cardiac Magnetic Resonance Imaging," *Magnetic Resonance in Medicine* 47 (2002): 372–383.

38. P. Kellman, A. E. Arai, E. R. McVeigh, and A. H. Aletras, "Phase-Sensitive Inversion Recovery for Detecting Myocardial Infarction Using Gadolinium-Delayed Hyperenhancement," *Magnetic Resonance in Medicine* 47 (2002): 372–383.

39. A. Tannús and M. Garwood, "Adiabatic Pulses," *NMR in Biomedicine* 10 (1997): 423–434.

40. M. Garwood and L. Delabarre, "The Return of the Frequency Sweep: Designing Adiabatic Pulses for Contemporary NMR," *Journal of Magnetic Resonance* 153 (2001): 155–177.

41. A. Tannüs and M. Garwood, "Improved Performance of Frequency-Swept Pulses Using Offset-Independent Adiabaticity," *Journal of Magnetic Resonance, Series A* 120 (1996): 133–137.

42. S. Rashid, S. Rapacchi, M. Vaseghi, et al., "Improved Late Gadolinium Enhancement MR Imaging for Patients With Implanted Cardiac Devices," *Radiology* 270 (2014): 269–274.

43. S. Rashid, S. Rapacchi, K. Shivkumar, A. Plotnik, J. P. Finn, and P. Hu, "Modified Wideband Three-Dimensional Late Gadolinium Enhancement MRI for Patients With Implantable Cardiac Devices HHS Public Access," *Magnetic Resonance in Medicine* 75 (2016): 572–584.

44. J. Shao, S. Rashid, P. Renella, K. L. Nguyen, and P. Hu, "Myocardial T1 Mapping for Patients With Implanted Cardiac Devices Using Wideband Inversion Recovery Spoiled Gradient Echo Readout," *Magnetic Resonance in Medicine* 77 (2017): 1495–1504.

45. P. Gut, H. Cochet, G. Caluori, et al., "Wideband Black-Blood Late Gadolinium Enhancement Imaging for Improved Myocardial Scar Assessment in Patients With Cardiac Implantable Electronic Devices," *Magnetic Resonance in Medicine* 92 (2024): 1851–1866.

46. M. S. Silver, R. I. Joseph, and D. I. Hoult, "Highly Selective and π Pulse Generation," *Journal of Magnetic Resonance (1969)* 59 (1984): 347–351.

47. T. Basha, S. Roujol, K. V. Kissinger, B. Goddu, W. J. Manning, and R. Nezafat, "Black Blood Late Gadolinium Enhancement Using Com-bined T2 Magnetization Preparation and Inversion Recovery," *Journal of Cardiovascular Magnetic Resonance* 17 (2015): 1–2.

48. P. Kellman, H. Xue, L. J. Olivieri, et al., "Dark Blood Late Enhancement Imaging," *Journal of Cardiovascular Magnetic Resonance* 18 (2016): 1–11.

49. A. T. O'Brien, K. E. Gil, J. Varghese, O. P. Simonetti, and K. M. Zareba, "T2 mapping in Myocardial Disease: A Comprehensive Review," *Journal of Cardiovascular Magnetic Resonance* 24 (2022): 33.

50. R. Nezafat, R. Ouwerkerk, A. J. Derbyshire, M. Stuber, and E. R. McVeigh, "Spectrally Selective B1-Insensitive T2 Magnetization Preparation Sequence," *Magnetic Resonance in Medicine* 61 (2009): 1326–1335.

51. P. T. Buser, W. Auffermann, W. W. Holt, et al., "Noninvasive Evaluation of Global Left Ventricular of Cine Nuclear Magnetic Resonance Function With Use," *Journal of the American College of Cardiology* 13 (1989): 1294–1300.

52. C. B. Higgins, W. Holt, P. Pflugfelder, and U. Sechtem, "Functional Evaluation of the Heart With Magnetic Resonance Imaging," *Magnetic Resonance in Medicine* 6 (1988): 121–139.

53. K. Scheffler and S. Lehnhardt, "Principles and Applications of Balanced SSFP Techniques," *European Radiology* 13 (2003): 2409–2418.

54. J. Schwitter, M. R. Gold, A. Al Fagih, et al., "Image Quality of Cardiac Magnetic Resonance Imaging in Patients With an Implantable Cardioverter Defibrillator System Designed for the Magnetic Resonance Imaging Environment," *Circulation: Cardiovascular Imaging* 9 (2016): e004025.

55. L. J. Olivieri, R. R. Cross, K. E. O'Brien, K. Ratnayaka, and M. S. Hansen, "Optimized Protocols for Cardiac Magnetic Resonance Imaging in Patients With Thoracic Metallic Implants," *Pediatric Radiology* 45 (2015): 1455–1464.

56. P. Rajiah, F. Kay, M. Bolen, A. R. Patel, and L. Landeras, "Cardiac Magnetic Resonance in Patients With Cardiac Implantable Electronic Devices: Challenges and Solutions," *Journal of Thoracic Imaging* 35 (2020): w1–w17.

57. T. Sasaki, R. Hansford, M. M. Zviman, et al., "Quantitative Assessment of Artifacts on Cardiac Magnetic Resonance Imaging of Patients With Pacemakers and Implantable Cardioverter-Defibrillators," *Circulation: Cardiovascular Imaging* 4 (2011): 662–670.

58. C. E. Raphael, V. Vassiliou, F. Alpendurada, S. K. Prasad, D. J. Pennell, and R. H. Mohiaddin, "Clinical Value of Cardiovascular Magnetic Resonance in Patients With MR-Conditional Pacemakers," *European Heart Journal – Cardiovascular Imaging* 17 (2016): 1178–1185.

59. S. Hilbert, C. Jahnke, S. Loebe, et al., "Cardiovascular Magnetic Resonance Imaging in Patients With Cardiac Implantable Electronic Devices: A Device-Dependent Imaging Strategy for Improved Image Quality," *European Heart Journal – Cardiovascular Imaging* 19 (2018): 1051–1061.

60. S. Löbe, I. Paetsch, S. Hilbert, et al., "Evaluation of the Right Heart Using Cardiovascular Magnetic Resonance Imaging in Patients With Cardiac Devices," *International Journal of Cardiology* 316 (2020): 266–271.

61. A. Barison, F. Ricci, A. G. Pavon, et al., "Cardiovascular Magnetic Resonance in Patients With Cardiac Electronic Devices: Evidence From a Multicenter Study," *Journal of Clinical Medicine* 12 (2023): 6673.

62. V. Holtstiege, C. Meier, M. Bietenbeck, et al., "Clinical Experience Regarding Safety and Diagnostic Value of Cardiovascular Magnetic Resonance in Patients With a Subcutaneous Implanted Cardioverter/Defibrillator (S-ICD) at 1.5 T," *Journal of Cardiovascular Magnetic Resonance* 22 (2020): 35.

63. A. M. Huber, S. O. Schoenberg, C. Hayes, et al., "Phase-Sensitive Inversion-Recovery MR Imaging in the Detection of Myocardial Infarction," *Radiology* 237 (2005): 854–860.

64. L. Jimenez Juan, A. M. Crean, and B. J. Wintersperger, "Late Gadolinium Enhancement Imaging in Assessment of Myocardial Viabil-

ity: Techniques and Clinical Applications," *Radiologic Clinics of North America* 53, no. 2 (2015): 397–411.

65. S. Rashid, A. Plotnik, H. Litt, et al., "Artifact Reduction With a Wideband Late Gadolinium Enhancement (LGE) MRI Technique for Patients With Implanted Cardiac Devices: A Two-Center Study," *Journal of Cardiovascular Magnetic Resonance* 16 (2014): 1–3.

66. A. Singh, K. Kawaji, N. Goyal, et al., "Feasibility of Cardiac Magnetic Resonance Wideband Protocol in Patients with Implantable Cardioverter Defibrillators and Its Utility for Defining Scar," *American Journal of Cardiology* 123 (2019): 1329–1335.

67. A. N. Bhuva, P. Kellman, A. Graham, et al., "Clinical Impact of Cardiovascular Magnetic Resonance With Optimized Myocardial Scar Detection in Patients With Cardiac Implantable Devices," *International Journal of Cardiology* 279 (2019): 72–78.

68. H. N. Patel, S. Wang, S. Rao, et al., "Impact of Wideband Cardiac Magnetic Resonance on Diagnosis, Decision-Making and Outcomes in Patients With Implantable Cardioverter Defibrillators," *European Heart Journal – Cardiovascular Imaging* 24 (2022): 181–189.

69. R. Ranjan, C. J. McGann, E. K. Jeong, et al., "Wideband Late Gadolinium Enhanced Magnetic Resonance Imaging for Imaging Myocardial Scar Without Image Artefacts Induced by Implantable Cardioverter-Defibrillator: A Feasibility Study at 3 T," *EP Europace* 17 (2015): 483–488.

70. A. Scatteia, S. Dellegrottaglie, M. Sinai Heart, and M. A. Wiener, "Cardiac Magnetic Resonance in Ischemic Cardiomyopathy: Present Role and Future Directions," *European Heart Journal Supplements* 25 (2023): C58–C62.

71. K. Thygesen, J. S. Alpert, A. S. Jaffe, et al., "Fourth Universal Definition of Myocardial Infarction (2018)," *Circulation* 138 (2018): e618–e651.

72. S. Kuruvilla, N. Adenaw, A. B. Katwal, M. J. Lipinski, C. M. Kramer, and M. Salerno, "Late Gadolinium Enhancement on Cardiac Magnetic Resonance Predicts Adverse Cardiovascular Outcomes in Nonischemic Cardiomyopathy: A Systematic Review and Meta-Analysis," *Circulation: Cardiovascular Imaging* 7 (2014): 250–257.

73. S. Toupin, T. Pezel, A. Bustin, and H. Cochet, "Whole-Heart High-Resolution Late Gadolinium Enhancement: Techniques and Clinical Applications," *Journal of Magnetic Resonance Imaging* 55 (2022): 967–987.

74. P. Garre, S. Vázquez-Calvo, E. Ferro, T. Althoff, and I. Roca-Luque, "Impact of LGE-MRI in Arrhythmia Ablation," *Applied Sciences* 13 (2023): 3862.

75. K. Hong, D. Lee, R. Sarnari, et al., "3D Isotropic Wideband LGE Pulse Sequence Using a Combination of Stack-of-Stars K-Space Sampling, 2D Self-Navigation, and XD-GRASP Reconstruction: A Preliminary Evaluation in Patients With an ICD," *Journal of Cardiovascular Magnetic Resonance* 26 (2024): 100921.

76. D. Andreu, J. T. Ortiz-Pérez, T. Boussy, et al., "Usefulness of Contrast-Enhanced Cardiac Magnetic Resonance in Identifying the Ventricular Arrhythmia Substrate and the Approach Needed for Ablation," *European Heart Journal* 35 (2014): 1316–1326.

77. D. Andreu, J. T. Ortiz-Pérez, J. Fernández-Armenta, et al., "3D Delayed-Enhanced Magnetic Resonance Sequences Improve Conducting Channel Delineation Prior to Ventricular Tachycardia Ablation," *Europace* 17 (2015): 938–945.

78. S. R. D. Piers, Q. Tao, M. De, et al., "CMR-Based Identification of Critical Isthmus Sites of Ischemic and Nonischemic Ventricular Tachycardia," *JACC Cardiovascular Imaging* 7 (2014): 774–784.

79. I. Roca-Luque, A. Van Breukelen, F. Alarcon, et al., "Ventricular Scar Channel Entrances Identified by New Wideband Cardiac Magnetic Resonance Sequence to Guide Ventricular Tachycardia Ablation in Patients With Cardiac Defibrillators," *Europace* 22 (2020): 598–606.

80. K. Hong, E. K. Jeong, T. S. Wall, S. G. Drakos, and D. Kim, "Wideband Arrhythmia-Insensitive-Rapid (AIR) Pulse Sequence for Cardiac T1 Mapping Without Image Artifacts Induced by an Implantable-Cardioverter-Defibrillator," *Magnetic Resonance in Medicine* 74 (2015): 336–345.

81. Y. S. Hamirani and C. M. Kramer, "Cardiac MRI Assessment of Myocardial Perfusion," *Future Cardiology* 10 (2014): 349–358.

82. X. M. Li, L. Jiang, C. Y. Min, et al., "Myocardial Perfusion Imaging by Cardiovascular Magnetic Resonance: Research Progress and Current Implementation," *Current Problems in Cardiology* 48 (2023): 101665.

83. H. Sakuma and M. Ishida, "Advances in Myocardial Perfusion MR Imaging: Physiological Implications, the Importance of Quantitative Analysis, and Impact on Patient Care in Coronary Artery Disease. Magnetic Resonance in Medical Sciences," *Japanese Society for Magnetic Resonance in Medicine* 21 (2022): 195–211.

84. T. Pezel, J. Lacotte, S. Toupin, et al., "Diagnostic Accuracy of Stress Perfusion CMR for Risk Stratification in Patients With MR-Conditional Pacemakers," *JACC Cardiovasc Imaging* 14 (2021): 2041–2054.

85. A. G. Pavon, A. P. Porretta, D. Arangalage, et al., "Feasibility of Adenosine Stress Cardiovascular Magnetic Resonance Perfusion Imaging in Patients With MR-Conditional Transvenous Permanent Pacemakers and Defibrillators," *Journal of Cardiovascular Magnetic Resonance* 24 (2022): 9.

86. L. Miller, S. Airapetov, A. Pillai, et al., "Hemodynamic Response and Safety of Vasodilator Stress Cardiovascular Magnetic Resonance in Patients With Permanent Pacemakers or Implantable Cardioverter-Defibrillators," *Journal of Cardiovascular Electrophysiology* 33 (2022): 2127–2135.

87. K. P. Hong, J. D. Collins, B. P. Knight, J. C. Carr, D. C. Lee, and D. Kim, "Wideband Myocardial Perfusion Pulse Sequence for Imaging Patients With a Cardiac Implantable Electronic Device," *Magnetic Resonance in Medicine* 81 (2019): 1219–1228.

88. K. Hong, J. D. Collins, B. H. Freed, et al., "Accelerated Wideband Myocardial Perfusion Pulse Sequence With Compressed Sensing Reconstruction for Myocardial Blood Flow Quantification in Patients With a Cardiac Implantable Electronic Device," *Radiology: Cardiothoracic Imaging* 2 (2020): e190114.

89. M. Penso, M. Babbaro, S. Moccia, et al., "Cardiovascular Magnetic Resonance Images With Susceptibility Artifacts: Artificial Intelligence With Spatial-Attention for Ventricular Volumes and Mass Assessment," *Journal of Cardiovascular Magnetic Resonance* 24 (2022): 62.

90. M. Villegas-Martinez, V. de Villedon de Naide, V. Muthurangu, and A. Bustin, "The Beating Heart: Artificial Intelligence for Cardiovascular Application in the Clinic," *Magnetic Resonance Materials in Physics, Biology and Medicine* 37 (2024): 369–382.